



This is a repository copy of *Order parameter and connectivity topology analysis of crystalline ceramics for nuclear waste immobilization*.

White Rose Research Online URL for this paper:
<http://eprints.whiterose.ac.uk/85385/>

Version: Accepted Version

Article:

Archer, A., Foxhall, H.R., Allan, N.L. et al. (5 more authors) (2014) Order parameter and connectivity topology analysis of crystalline ceramics for nuclear waste immobilization. *Journal of Physics: Condensed Matter*, 26 (48). ISSN 0953-8984

<https://doi.org/10.1088/0953-8984/26/48/485011>

Reuse

Unless indicated otherwise, fulltext items are protected by copyright with all rights reserved. The copyright exception in section 29 of the Copyright, Designs and Patents Act 1988 allows the making of a single copy solely for the purpose of non-commercial research or private study within the limits of fair dealing. The publisher or other rights-holder may allow further reproduction and re-use of this version - refer to the White Rose Research Online record for this item. Where records identify the publisher as the copyright holder, users can verify any specific terms of use on the publisher's website.

Takedown

If you consider content in White Rose Research Online to be in breach of UK law, please notify us by emailing eprints@whiterose.ac.uk including the URL of the record and the reason for the withdrawal request.



eprints@whiterose.ac.uk
<https://eprints.whiterose.ac.uk/>

**Order Parameter and Connectivity Topology Analysis of Crystalline Ceramics
for Nuclear Waste Immobilisation**

Adam Archer¹, Henry R. Foxhall², Neil L. Allan¹, David S.D. Gunn³, John H.
Harding², Ilian T. Todorov³, Karl P. Travis², and John A. Purton³

¹ School of Chemistry, University of Bristol, Cantock's Close, Bristol, BS8 1TS, UK

² Department of Materials Science and Engineering, University of Sheffield, S1 3JD,
UK.

³ STFC, Daresbury Laboratory, Keckwick Lane, Daresbury, WA4 4AD, UK.

Abstract

We apply bond order and topological methods to the problem of analysing the results of radiation damage cascade simulations in ceramics. Both modified Steinhardt local order and connectivity topology analysis techniques provide results that are both translationally and rotationally invariant and which do not rely on a particular choice of a reference structure. We illustrate the methods with new analyses of molecular dynamics simulations of single cascades in the pyrochlores $\text{Gd}_2\text{Ti}_2\text{O}_7$ and $\text{Gd}_2\text{Zr}_2\text{O}_7$ similar to those reported previously (Todorov et al 2006 *J. Phys Condes. Mat.* **18** 2217). Results from the Steinhardt and topology analyses are consistent, while often providing complementary information, since the Steinhardt parameters are sensitive to changes in angular arrangement even when the overall topological connectivity is fixed. During the highly non-equilibrium conditions at the start of the cascade, both techniques reveal significant localised transient structural changes and variation in the cation-connectivity. After a few picoseconds, the connectivity is largely fixed, while the order parameters continue to change. In the zirconate there is a shift to the anion disordered system while in the titanate there is substantial reversion and healing back to the parent pyrochlore structure.

Introduction

A long-term goal in nuclear waste disposal^{1,2,3} is inert matrix materials that retain structural integrity when subjected to prolonged radiation damage. In particular, materials with the pyrochlore structure are of considerable interest as host matrices for plutonium, arising from dismantling of atomic weapons and spent fuel-reprocessing operations. Even if a large proportion of stored PuO₂ is to be used in mixed oxide (MOX) fuel, conversion of any remaining or contaminated PuO₂ into a proliferation resistant and environmentally stable form by immobilisation in a host material matrix is still required. Many radioactive wastes, including (non Pu-containing) high-level waste liquors from reprocessing operations in the UK are immobilised in an alkali-borosilicate glass matrix, but the low solubility of plutonium in glass⁴ renders it less suitable for PuO₂ immobilisation. Crystalline matrices have been cited as suitable immobilisation materials for Pu, particularly the SYNROC C multiphase assemblage,^{3,5} which includes monoclinic zirconolite, CaZrTi₂O₇ and as well as a TiO₂ buffer phase. Pyrochlore-structured phases are seen upon synthesis of actinide-containing zirconolite, Ca(Zr_{1-x}Act_x)Ti₂O₇ in cases where $x > 0.4$.⁶ Understanding radiation damage in host-matrix materials at the atomic level is an important part of implementing them for long-term storage of actinide wastes. For example, Wang et al.⁷ have used heavy ion bombardment to highlight the striking variation in radiation tolerance in the series Gd₂(Zr_xTi_{1-x})₂O₇ ($0 < x < 1$). Increasing Zr content is accompanied by a dramatic increase in predicted radiation tolerance, leading to lifetime predictions across the compositional series ranging from 800 to 3×10^6 years.⁸ Gd₂Ti₂O₇ undergoes a radiation-induced crystalline-amorphous transition yielding a metamict state,^{7,9} whereas the behaviour of Gd₂Zr₂O₇ under the same conditions is quite different, transforming to a defect fluorite structure. Gd₂Ti₂O₇ is one of the most susceptible to ion irradiation-induced amorphisation of the rare-earth titanate pyrochlores. This is unfortunate, as the SYNROC C related titanate phases, betafite (Ca,U)Ti₂O₇¹⁰ and zirconolite CaZrTi₂O₇¹¹ are principal candidates for Pu-immobilization through having displayed desirable longevity in geological environments (despite being found as metamict phases). Due to its relationship to these phases Gd₂Ti₂O₇ is a useful model material. The detailed underlying reasons for variations in properties between compositionally similar pyrochlores must lie in the

atomic-level behaviour and this remains the subject of much attention and conjecture (for a short recent overview see ref. 12,13,14).

Upon emission of an alpha particle, the emitting isotope recoils in the opposite direction and is termed a Primary Knock on Atom (PKA). The large mass of an actinide PKA is responsible for many thousands of atomic interactions, introducing defects and disorder to the system to an extent that varies considerably with the nature of the host material. Many studies of defect formation in materials for nuclear waste immobilisation have been presented in the literature (e.g. refs. 15-24) in which various techniques and scales are seen, one of which is molecular dynamics (MD), which is a powerful tool as it probes the very length and time scales of interest in radiation damage studies. Examples are those of Chartier et al.¹⁸, Devanathan²⁵ and pyrochlore studies by Purton and co-workers.^{8,24,26} Very large (several-million-atom) damage cascade simulations have been performed by Trachenko and co-workers²⁷ These large cascade simulations push the boundaries of MD to the limit of current computational resources.

Work here is concerned with the analysis of large datasets from such simulations to discover the nature of the large-scale damage or disorder introduced by the cascades. This is non-trivial, especially as many thousands or even millions of atoms may be involved. Using the results from MD simulations of damage cascades in the pyrochlores $Gd_2Ti_2O_7$ and $Gd_2Zr_2O_7$ similar to those reported in earlier work⁸ we discuss critically the limitations of previous methods, before turning to two techniques, novel in their application to radiation damage simulations. The first is based on averaged Steinhardt bond-order parameters²⁸, and the second is connectivity topology^{22,29}, a symmetry-independent technique based on graph theory. We present structural characterisations using both techniques and compare the results from each. In the final section of the paper we discuss the more general implications for simulating and understanding radiation damage in pyrochlores and related materials.

The pyrochlore structure (space group $Fd\bar{3}m$), shortened to PYR in our discussion, is closely related to that of fluorite (space group $Fm\bar{3}m$) and is shown in Figure 1. Cations with 3+ (Gd) and 4+ charges (Ti, Zr) occupy the 16d and 16c sites respectively. Oxide ions at the 48f position have two 3+ and two 4+ nearest cation neighbours; those at the 8b site are surrounded by four 3+ cations. The vacant 8a site also has four 4+ cation neighbours. The 3+ cations and 4+ cations are eightfold and sixfold coordinate to oxygen respectively. An important difference between the two pyrochlores considered in this paper is that there is intrinsic oxide ion disorder in

$Gd_2Zr_2O_7$ involving partial occupancy of this 8a site and experimentally enhanced ionic conductivity is observed; in contrast the intrinsic disorder and ionic conductivity of $Gd_2Ti_2O_7$ are negligible.³⁰

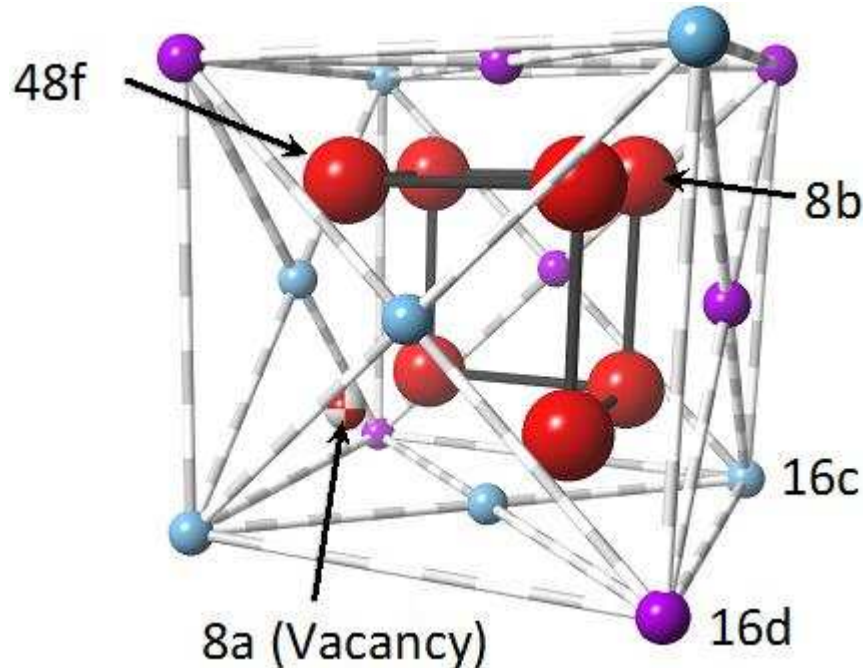


Figure 1 One-eighth of the unit cell of the pyrochlore (PYR) $Gd_2M_2O_7$ ($M=Ti,Zr$) structure. Gd^{3+} ions are purple, Ti/Zr^{4+} ions are blue and O^{2-} ions are red. The anion vacancy is shown as a beach ball design.

The defect fluorite (DF) structure is closely related to that of pyrochlore but with a random distribution of the two different cations over the cation lattice sites and random occupancy of the anion sub-lattice over 8a and 8b sites. Since the oxide ions are much more mobile than the cations, we also consider a solely anion-disordered pyrochlore (ADP) structure, which retains cation ordering as in the pyrochlore structure, but possesses a randomized anion sub-lattice. It is also useful to define two intermediate structures between these various possibilities which we label INT1 and INT2. INT1 is 20% ADP in which the cubic ADP “core” is surrounded by pure pyrochlore. INT2 is 20% DF in which the cubic DF “core” is surrounded by ADP. The order parameters of INT1 and INT2 are heavily influenced by the internal interfaces present between the different phases. This is not so for the topological analysis which depends solely on connectivity rather than (bond) angles.

Here, the emphasis is on the use of the analysis tools in the simulations, rather than on the pyrochlores themselves, the chemistry of which will be considered in more detail elsewhere using new interatomic potentials recently suggested by Gunn et al.³¹

Analysis of radiation damage

Traditional methods

Traditionally, a key observable for modelling radiation damage is the number of defects present in the structure before, during and after an alpha-recoil radiation damage event. It is straightforward to monitor the displacement, x , of atoms during a cascade and define a set radial displacement, r , beyond which a displaced ion is considered a “defect”. The value of r has previously been set to half of the average first neighbour interatomic distance.³² For complex ceramic structures, and specifically here for the pyrochlore structure, the definition of a cut-off distance in terms of nearest neighbours is non-trivial, but regardless, the number of “defects” decreases with increasing cut-off and qualitative differences between the defect populations for $\text{Gd}_2\text{Ti}_2\text{O}_7$ and $\text{Gd}_2\text{Zr}_2\text{O}_7$ do not change for any reasonable choice $> 1 \text{ \AA}$.⁸ This approach suggests that many more anions are displaced in the Zr pyrochlore than the Ti at any stage of the simulation, consistent with the well-established high anion mobility in the Zr compound and partial occupancy of the 8a site in the pyrochlore structure. However, many displaced anions end up occupying equivalent crystallographic sites or the 8a position. Thus simply counting atomic defects defined in this way is not very informative.

A related technique of characterising the extent of damage in molecular dynamics simulations uses a spherical method⁸, where atomic positions, for example, in a simulation cell are compared with those in a fixed reference structure. Any atom residing more than a set distance from an atomic site is termed an interstitial defect leaving a vacancy behind to form a Frenkel pair. An antisite defect is an atom residing within a set distance of an atomic site other than the one where it began. The values obtained using the output from the simulations of $\text{Gd}_2\text{Zr}_2\text{O}_7$ and $\text{Gd}_2\text{Ti}_2\text{O}_7$ show the same trends as those obtained using the simple displacement criterion above. Unfortunately, it is difficult to define with any rigour the site of a vacancy in the

reference structure, such as the 8a position in the pyrochlore and when the reference structure is already formally disordered, such as in DF, this becomes impossible. It is also non-trivial to assess the effect of disorder in constant pressure simulations where the volume of the simulation cell is free to change and non-uniform distortions and deformations occur throughout the material during radiation damage. This local lattice distortion may lead to ions being classified as interstitial defects even though no bonds are broken. The spherical method is thus likely to over-estimate, often severely, the numbers of defects formed in a collision cascade. In the Wigner-Seitz method^{33,34} the number of atoms in a Wigner-Seitz cell is counted, which also requires the use of a reference structure.

A natural alternative to tracking vacancies in the material is to monitor the radial distribution functions throughout a cascade simulation. This has been considered previously for $\text{Gd}_2\text{Ti}_2\text{O}_7$ and $\text{Gd}_2\text{Zr}_2\text{O}_7$ and can be instructive.⁸ Unfortunately however, the differences are small since the interatomic separations involved in the immediate coordination sphere around any given ion are, on the whole, largely preserved, and one must resort to integrating the absolute values of the areas under the difference curves. This integration indicates a larger loss of order in the Zr pyrochlore at shorter separations (3-5 Å)⁸ whereas at larger distances there appears to be a slightly larger loss of order for the Ti compound.

Improved methodologies

This paper is primarily concerned with assessing disorder on an atomic-scale. To generate suitable datasets we have used MD simulations of cascades in $\text{Gd}_2\text{Ti}_2\text{O}_7$ and $\text{Gd}_2\text{Zr}_2\text{O}_7$ similar to those reported previously⁸ but using a larger simulation cell and more energetic PKAs. These used the DL-POLY 3 code³⁵, a set of electron-gas potentials all fitted to a single exponential term⁸, PKAs with energies of 30 keV and cubic simulation cells containing 937,024 atoms. The length of the simulation cell was set to be the appropriate multiple (22) of the experimental lattice parameter, the initial temperature was 300 K and equilibration (before the damage event) was performed for 10 ps in the NPT-ensemble with a timestep of 2 fs. All cascade simulations were on the NVE ensemble with a U^{3+} ion replacing a Gd^{3+} ion as the PKA. This ion was set moving in the [111] direction by assigning to it an excess kinetic energy equivalent to the chosen recoil energy. A variable timestep was used for the cascade simulations to ensure that during the highly non-equilibrium early stages of the cascade, the timestep

was sufficiently short to allow for the presence of fast moving, highly energetic atoms, while maintaining overall resource efficiency. The total length of the cascade simulations were 110 and 100 ps for $\text{Gd}_2\text{Ti}_2\text{O}_7$ and $\text{Gd}_2\text{Zr}_2\text{O}_7$ respectively; although we shall see that in fact very few changes are seen after approximately 15 ps.

Steinhardt order parameters and their modification

Local bond-order or Steinhardt order parameters²⁸ are often used to distinguish between crystalline structures and polytopes, (e.g ref 36) and also to characterise non-stoichiometric grain boundaries.³⁷ The parameters are independent of the reference frame used to specify the crystal structure, i.e. they are translationally and rotationally invariant. An atom i is selected from the structure. For each vector \mathbf{r} which connects this atom i to those within a given cut-off distance (the primary cut-off), a set of even-order spherical harmonics³⁸ Q_{lm} are calculated:

$$Q_m(\mathbf{r}) = Y_{lm}(\theta(\mathbf{r}), \phi(\mathbf{r})) \quad (1)$$

where θ and ϕ are the polar angles defining the orientation of \mathbf{r} . The average value of Q_{lm} over the N_b neighbours within the cut-off distance is:

$$Q_{lm}(i) = \frac{1}{N_b(i)} \sum_{j=1}^{N_b(i)} Q_{lm}(j) \quad (2)$$

To obtain a rotationally invariant quantity we now average over all possible values of m for a given l to obtain the quantity $Q_l(i)$:

$$Q_l(i) = \sqrt{\frac{4\pi}{2l+1} \sum_{m=-l}^l |Q_{lm}(i)|^2} \quad (3)$$

There are large numbers of atoms associated with damage cascades, and our eventual goal is to assign local structures surrounding individual atoms. Thus we calculate a further average of $Q_l(i)$ over all the atoms i in spherical regions of radius 12 \AA (the secondary cut-off distance) each centred on one of the atoms in the simulation cell, finally obtaining a value of Q_l for each region. We refer to such regions as secondary spheres. We can also average only the Q_l for all regions centred on a particular atom type (Gd,Ti/Zr,O) to obtain $Q_l(\text{Gd})$, $Q_l(\text{Ti/Zr})$ and $Q_l(\text{O})$. Lechner and Dellago³⁹ in their study of soft particle systems carried out a similar procedure but first averaged the Q_{lm} parameter. As with the measures used by these authors, we have found that, although this final averaging stage reduces the spatial resolution, it is helpful in increasing the accuracy of the distinction of different structures.

We use primary and secondary cut off distances of 3.2 Å and 12 Å respectively. The primary distance is such that just nearest neighbours are included in the calculation of the individual Q_{lm} for both compounds, as confirmed by the cation-anion radial distribution functions shown in Figure 2. We summarise the overall procedure in the flow diagram in Figure 3.

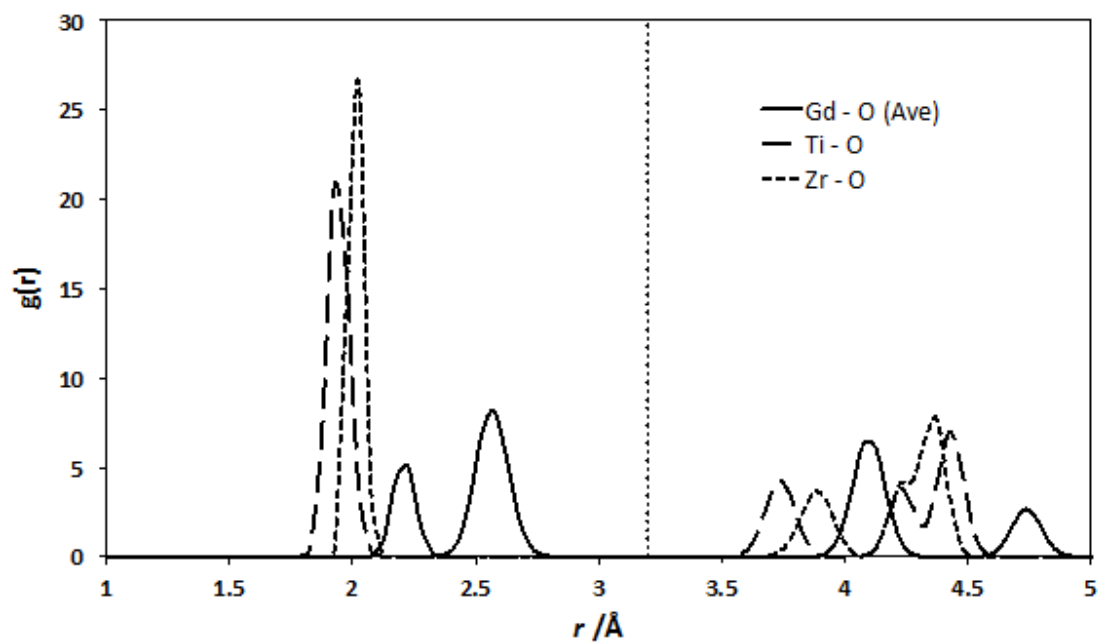


Figure 2 Partial cation-anion radial distribution functions, $g(r)$, for cation-anion pairs in the equilibrated zirconate and titanate pyrochlores. Also shown is the 3.2 Å nearest neighbour cut-off employed for the Steinhardt order parameter calculations and the topological analysis.

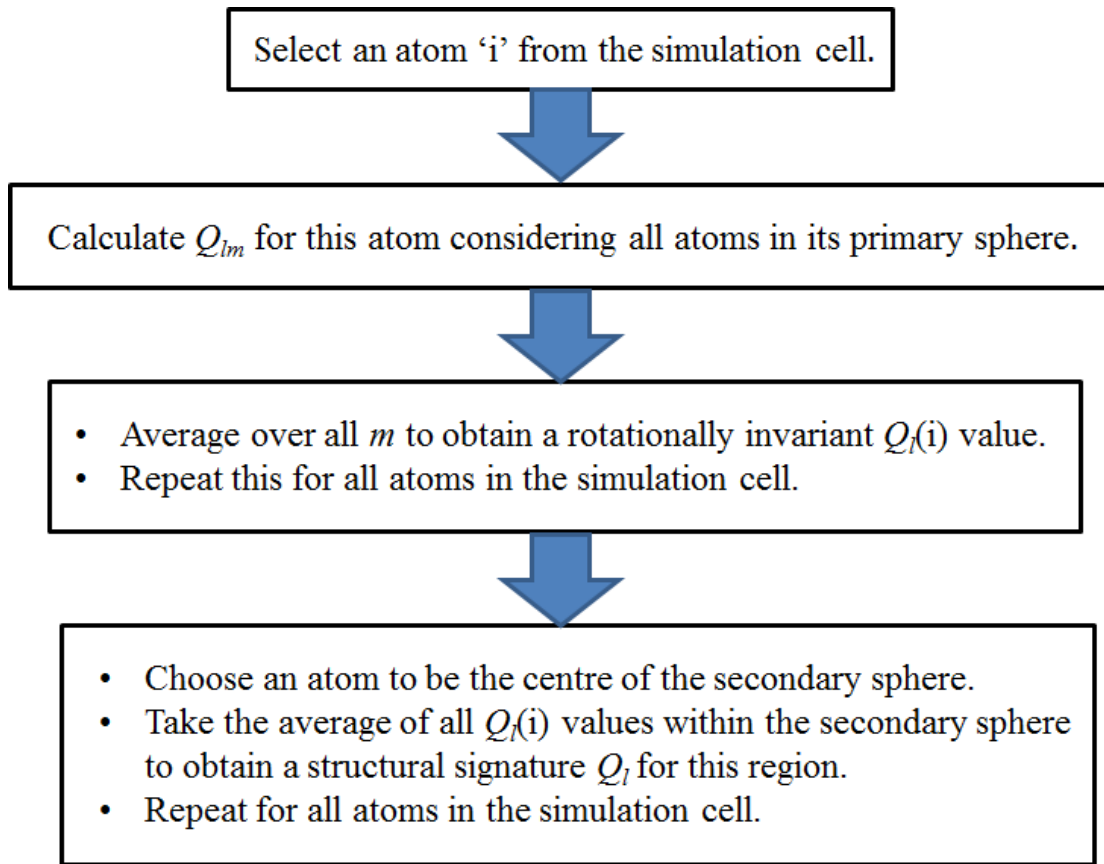


Figure 3 Flow-chart for the evaluation of Q_1 .

We have carried out a large number of analyses with different choices of primary and secondary cut-offs. We managed to determine the values needed to produce consistent, converged and structurally sensitive results for any sensible choice of sphere origin without excessive computational cost. For the secondary cut-off, we show in Figure 4 the variation of the mean and standard deviation of the Q_6 probability distribution as a function of cut-off for a typical cascade in $\text{Gd}_2\text{Ti}_2\text{O}_7$.

Here, we consider both average analyses over the entire simulation cell, and also averages of selected volume of crystal local to the PKA track and centre of the damage cascade in order to compare more closely with the topological analysis.

Although it would be possible to evaluate analogous Q_1 indices considering only cation-cation, anion-anion or cation-anion atom pairs, we have chosen to include all ions in the evaluation.

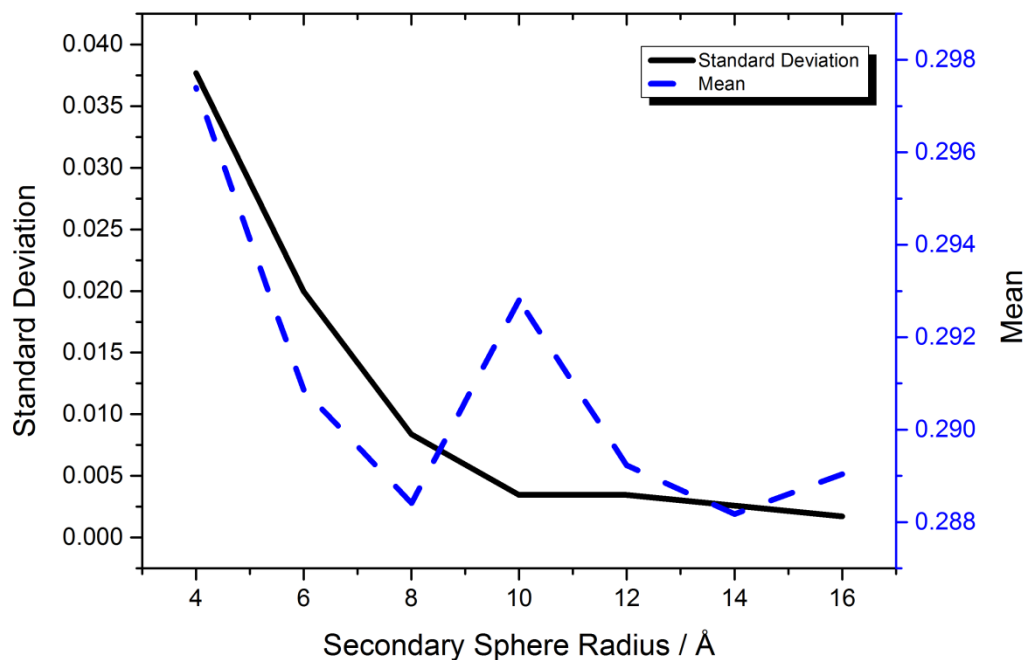


Figure 4 Mean and standard deviation of the Q_6 probability distribution vs. secondary cut-off for $Gd_2Ti_2O_7$.

Connectivity Topology (CT) Analysis

CT analysis, based on graph theory, is also a powerful method of defining structural changes in disordered crystals using a system of connectivity and nearest-neighbour searches and is suitable for characterisation and identification of defective and disordered systems as the introduction of defects changes the network of connectivity in, and therefore the topological signature of, the system. Unlike the Steinhardt parameter, it is purely a distance-based analysis, and takes no account of angle. It is invariant to translation and rotation and due to its non-reliance on a pre-determined reference structure it can therefore account for lattice and polyhedral distortion. We show later that the ability to use both techniques in tandem provides us with significant advantages when examining the structural effects of radiation damage, as the connectivity and the angular distribution of the atoms do not necessarily alter at the same time as each other.

CT analysis documents connectivity paths throughout a system and defines a ring as being a closed connectivity path that does not intersect itself. Each ring has an

order defined by the number of vertices in that ring. Closed rings or paths are a steric necessity in graphs representing real atomic systems at fixed density, as any path must close to avoid a density catastrophe, which would otherwise occur due to exponential growth in connection numbers seen in an open (or ‘tree’) graph. One can further define a primitive ring as one with no shortcut, or alternatively a ring that cannot be decomposed into two smaller rings.⁴⁰ The set of atoms contained in all primitive rings starting and finishing at a chosen focus atom is termed the local cluster, and provides us with a topological signature for a chosen focus atom. In a perfect crystal at equilibrium this is the topological repeat unit, analogous to a unit cell in standard crystallography, and is identical for all equivalent crystallographic sites. In defective or disordered materials, it provides a method of comparison between localised regions of atomic structure. For CT analyses (based once again on the radial distribution functions presented in Figure 3) radial nearest neighbour cut-offs for all cation-anion connections were set at 3.2 Å, while cut-offs for cation-cation and anion-anion interactions were set to zero to preclude any connectivity.

Results and Discussion

Signatures of crystalline pyrochlore (PYR), anion-disordered pyrochlore (ADP), defect fluorite (DF) and intermediate structures

Any method used for analysis of radiation-damaged pyrochlore materials must be able to distinguish locally between different structures, so, before considering the complex situations accompanying radiation damage one must construct signatures for each structure to be used in the subsequent assignment.

We start with a consideration of the Steinhardt parameters for equilibrium $\text{Gd}_2\text{Ti}_2\text{O}_7$ and $\text{Gd}_2\text{Zr}_2\text{O}_7$ structures. Figures 5a & 5b show, for example, the order parameters Q_l ($l=4,6,10$) evaluated for $\text{Gd}_2\text{Ti}_2\text{O}_7$ and $\text{Gd}_2\text{Zr}_2\text{O}_7$ respectively for the PYR, ADP and DF structures, and the two intermediates INT1 and INT2 which are discussed in the introduction. For both compounds we have found it sufficient to work only with Q_4 , Q_6 and Q_{10} , as together they provide sufficient information to assign a structural type to any region of material. Each plot tracks the distribution of order parameters over the course of a dynamics run of 0.1 ns for a particular system with a simulation cell of 937,024 atoms.

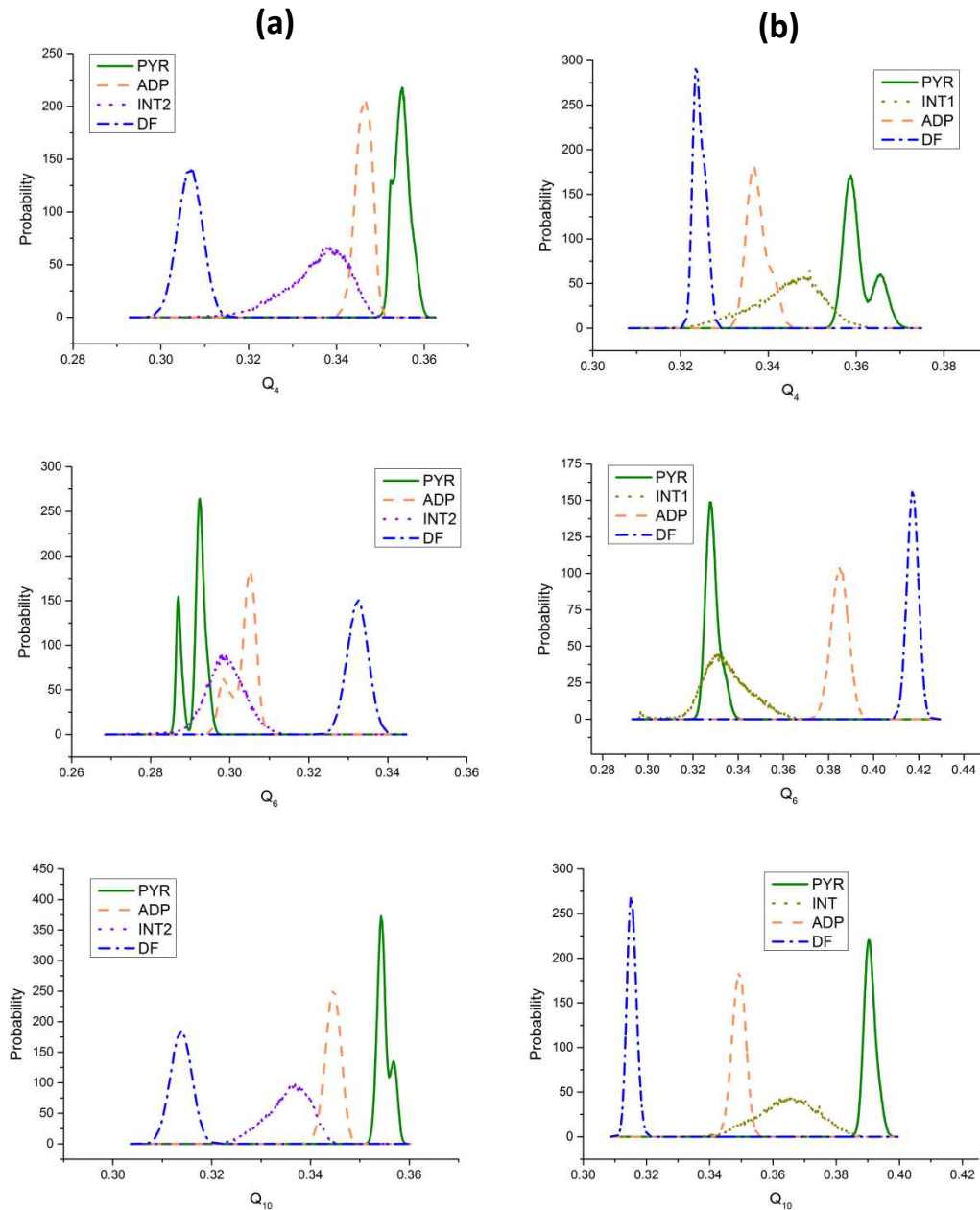


Figure 5a and 5b Order parameters Q_4 , Q_6 , and Q_{10} evaluated for (a) $\text{Gd}_2\text{Ti}_2\text{O}_7$ (as PYR, ADP, DF, INT2) and (b) $\text{Gd}_2\text{Zr}_2\text{O}_7$ (as PYR, ADP, DF, INT1, INT2). PYR=pyrochlore, ADP=anion-disordered pyrochlore, DF = defective fluorite, and INT1 and INT2 are the intermediate structures discussed in the text. The curves have been normalised such that the relative areas under each curve is equal to one.

We require a method of assigning a structural type to a secondary sphere in the damaged system given a particular set of values of the parameter Q_1 , and there is no unique procedure for this. When the order parameters fall in a region where there is only one Q_1 curve from the different possibilities, the choice is trivial. However, if a calculated index lies in a region where several Q_1 curves overlap, it could apply to

multiple structures and in this case we assign it to the strongest structural signal. For example, a Q_4 value of 0.34 for $Gd_2Zr_2O_7$ in Fig. 5b is classified as ADP. A structural type can only be assigned to a region if at least two of the three indices for a particular secondary sphere give the same result. Otherwise the region is assigned a label of “amorphous/other”, which for simplicity we abbreviate to “amorphous”. For values lying outside the regions corresponding to any of the five structures (i.e., outside the limits on the x-axes in Figures 5a & 5b) then the “amorphous” label is also applied. There is an unavoidable degree of arbitrariness about this classification scheme, but through experience we are confident that errors due to incorrect assignment are negligible.

In CT analysis of crystalline materials, we obtain site-specific topological signatures and this is presented for PYR in Table 1. They are identical for both Ti and Zr compounds in all three structural types as topology deals purely with angle-independent connectivity (note that connectivity is not necessarily equal to classically envisaged chemical bonding in the material) and the choice of radial search cut-off encompasses all bond length variations in both materials. Also included in the crystalline signatures (and useful in some cases for distinguishing between similar crystalline structures) are the individual ring permutations within these populations. The even distribution of 4-rings between cation sites highlights the ordered nature of PYR while the uneven distribution of 8-ring permutations arises from the vacant 8a site. There are no rings of order-10 or greater in PYR at equilibrium.

Due to the random ordering of one or both sublattices in ADP (anion) and DF (cation and anion) respectively, the final structure and hence topological signature depends on the particular structure considered. We therefore use an average value obtained from the averaging of signatures over 8 DF and 8 ADP structures. Note that, in contrast to CT analysis, the order parameters are sensitive to the different angular relationships in Ti and Zr compositions and therefore the set of Q_i are different in each case.

Central Atom	Ring Order	Details
A	4	6 x A-O-A-O
		6 x A-O-B-O
	6	12 x A-O-A-O-B-O
		6 x A-O-A-O-A-O
	8	11 x A-O-B-O-B-O-A-O
		13 x A-O-A-O-B-O-B-O
B	4	6 x B-O-A-O
		6 x B-O-A-O-A-O
	6	6 x B-O-B-O-B-O
		12 x B-O-B-O-A-O-A-O
	8	12 x B-O-A-O-A-O-B-O

Table 1 Ring details for local clusters in $A_2B_2O_7$ pyrochlore.

In the ADP structure, ions are randomised across the 8a and 8b sites of the anion sub-lattice, and additionally for DF, the cation sub-lattice is also randomised. As the chosen connectivity cut-offs for all cation-anion connections are equal, we cannot therefore distinguish between ADP, DF and INT2 (20% DF, 80% ADP) structures using CT analysis, and require further confirmation via angular dependent order-parameter techniques. As expected, the INT1 (20% ADP, 80% PYR) signature lies between PYR and ADP.

Central Atom	Ring Order	Average Topological Signature		
		PYR	INT1	ADP/DF
A	4	12.0	11.4	9.4
	6	18.0	17.6	16.5
	8	24.0	24.8	26.2
	10	0.0	0.007	0.06
B	4	6.0	6.58	8.5
	6	12.0	12.9	15.7
	8	24.0	24.8	26.2
	10	0.0	0.005	0.06

Table 2 Ring details for local clusters in PYR, INT1, and the ADP/DF structures. Rings with order > 10 were not seen in any structures before radiation damage. In the pyrochlore structure the central atom A is Gd, and the central atom B is Ti/Zr.

Radiation damage in $Gd_2Ti_2O_7$ Pyrochlore

Results obtained for the modified Steinhardt parameters Q_l for the relative abundance of the different structural types during the first 25 ps of a cascade are shown in Figure 6a. Pyrochlore is not shown in this figure because its abundance is never less than 94% and so it would dwarf the plot. The decay event takes place at $t = 0$. In this figure the entire simulation cell of 937,024 atoms is used to calculate the Q_l . There is a rapid increase in the amounts of ADP (to over 5%), which then diminishes to less than 1%. Overall there is reversion from ADP to PYR, consistent with the absence of a known DF phase for the Ti compound in nature, and the observed absence of oxygen conductivity suggesting a preference of the oxide ions for PYR-type positions.

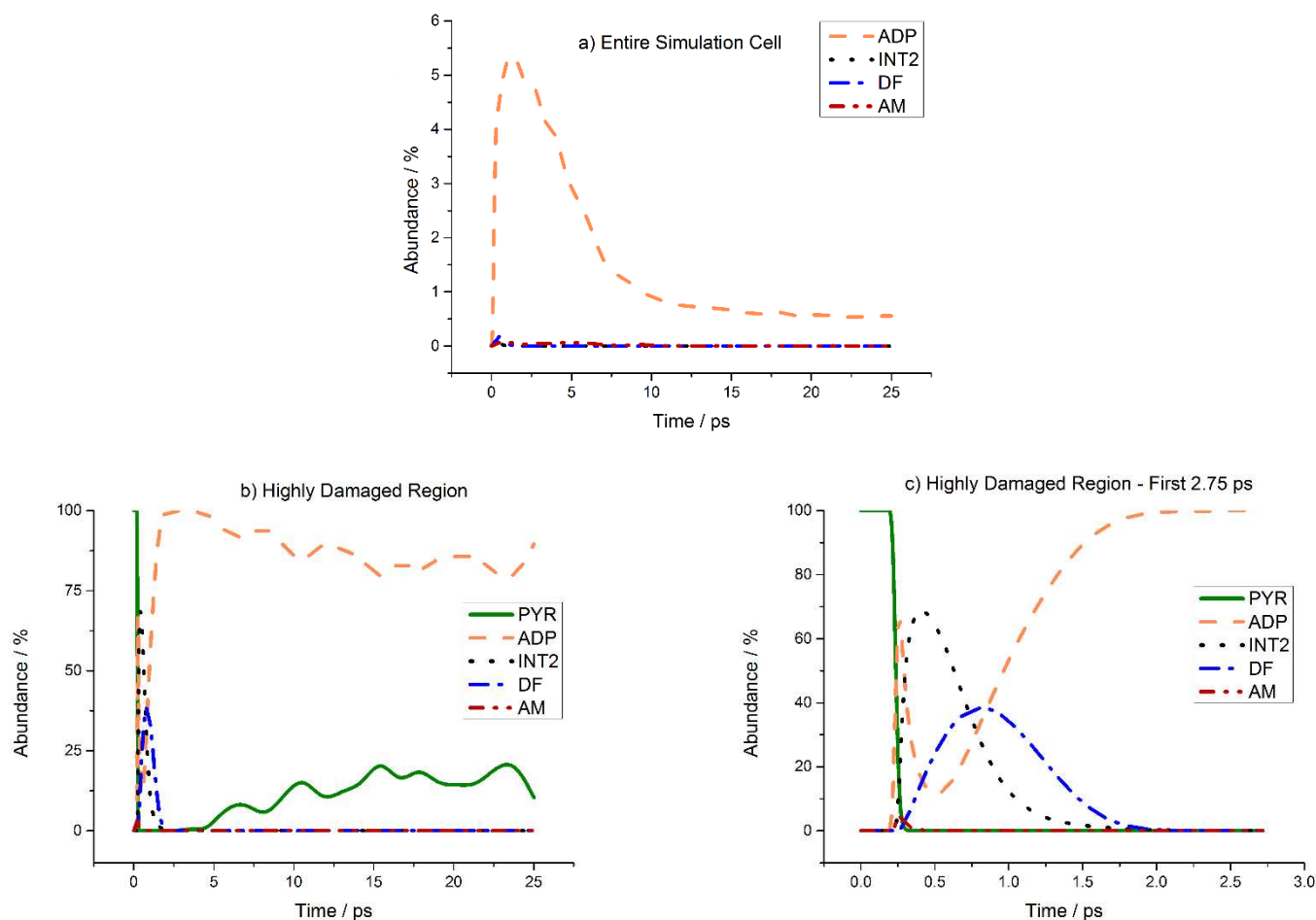


Figure 6 The relative abundance of pyrochlore (PYR), anion-disordered pyrochlore (ADP), defect fluorite (DF), the intermediate (INT2) and the amorphous (AM) structures in $\text{Gd}_2\text{Ti}_2\text{O}_7$ as a function of time determined by Steinhardt order parameter analysis (a) in the entire simulation cell, (b) in a cubic box of side 14 \AA taken from a highly damaged part of the cell as described in the text and (c) the first 2.75 ps of the simulation in this highly damaged area. PYR is not shown in frame (a) since its abundance is never below 94%.

Figure 6b is analogous to Figure 6a but considers the most highly damaged part of the simulation cell, specifically a cubic cell of side 14 \AA centred on the PKA track at the point where the cascade possessed the greatest cross-sectional area perpendicular to the PKA track. For this purpose, cascade size is defined as the volume of crystal in which atoms are displaced further than the first neighbour peak in the radial distribution function. The population of displaced atoms is largest at 1.4 ps, and at this time the width of the cascade perpendicular to the initial PKA direction is measured at various

points along the PKA track. At the point where the width was greatest, the midpoint of the distance from one edge to the other was taken as the centre of the 14 Å analysis cube. The size of the cube was fixed at the point of maximum damage and then these dimensions used throughout the simulation.

Now we see details obscured in Figure 6a. Almost immediately after the decay event, the oxygens move extensively and 90% of this smaller region is ADP. The cations then disorder and the ADP transforms to DF, all within less than approximately 0.1 ps. Healing now begins and we see the formation of ADP once again, but this time the growth of this structure is from DF or INT2 (i.e., ADP surrounding DF) as the cations reorder. Almost all this part of the cell is ADP from this point up to 5 ps, after which PYR begins to reform as the ADP heals and the oxygen anions reorder. There is little amorphisation at any stage.

Figure 7 shows the entire cell and those regions where the averaged Q_1 indicates a local ADP (orange) or amorphous (red) region during the course of 13 ps after the damage event. Regions that are pyrochlore are not shown. Along the path of the PKA there is a track consisting largely of ADP and, consistent with the plots of structural signatures and the timescales in Figure 6, the amount of ADP increases before it heals back to PYR.

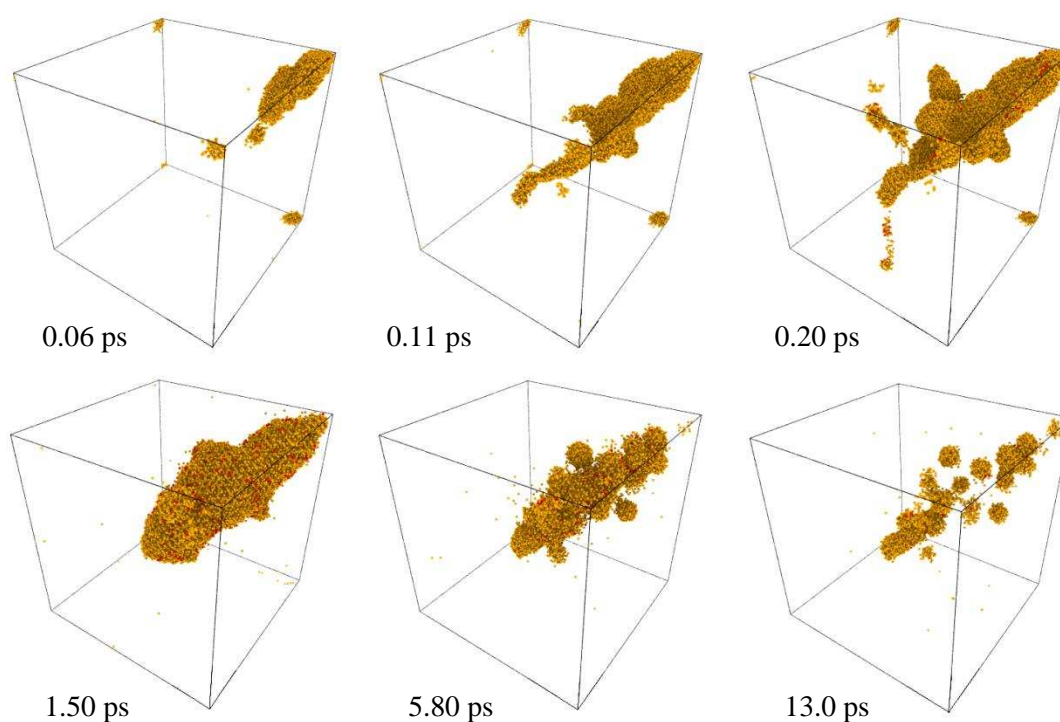


Figure 7 Analysis of selected frames of the cascade in $\text{Gd}_2\text{Ti}_2\text{O}_7$ at 0.06, 0.11, 0.20, 1.5, 5.8 and 13 ps. Each orange sphere represents a spherical region with a radius of 12 Å in which the dominant structure is ADP as indicated by the Q_1 values. Red denotes amorphous. Regions that are pyrochlore are not shown. Note that the damage does not spread beyond two-thirds of the diagonal length - no damage re-enters the simulation box.

Turning to the topological analysis, Figure 8 plots the variation in CT signatures for rings of order 4, 6 and 8 over time, averaged over all Gd or Ti atoms in the same local volume of cascade used above in the generation of Figure 6b. Computational constraints prohibit an average topological signature of the entire million atom simulation cell.

The topological signature observes changes in connectivity whereas Steinhardt parameters assess angular rearrangement. These do not necessarily occur over the same timescale and, usually, as here, the latter continues after the former has ceased. For the first 2 ps there are transient changes in topological signature which are short-lived, are difficult to quantify and quickly subside. Further connectivity changes depend on cation type. At 3 ps for Ti, the effects of the cascade diminish and there is little alteration in the signature, which is close to that of PYR, thereafter. For Gd, the topological signatures are still changing up to approximately 8 ps, as shown by the changes in the population of 6- and 8-rings. While the average population of 8-rings for Gd returns to the PYR value, the populations of 4- and 6-rings suggest an intermediate structure, consistent with the trends in Table 2. The Gd connectivity and possibly the Ti 6-ring population indicate a shift to a disordered anion sub-lattice.

For Ti, unlike Gd, a permanent change in the number of 4-rings is not seen, suggesting the immediate local topological environment is not changing after the first 2 ps of the cascade. This is despite some rearrangement of the $[\text{TiO}_x]$ polyhedral units themselves, as reflected in the variation in the 6- and 8-ring populations, which overall move slightly to PYR. Any anion disorder introduced is largely associated with the connectivity of the Gd atoms, while the Ti atoms retain their immediate octahedral coordination. This is consistent with the relative bond strengths: Gd-O is weaker than Ti-O.

The $[\text{GdO}_x]$ polyhedra distort to accommodate the rearrangement of the TiO_6 octahedra, and the Steinhardt analysis is more sensitive to these changes. The connectivity is largely fixed but the angular location of anions in the immediate

surrounding environment is changing. The two analyses together tell us that polyhedral rearrangement is being seen – consistent with previous studies of radiation damage in titanates.²²

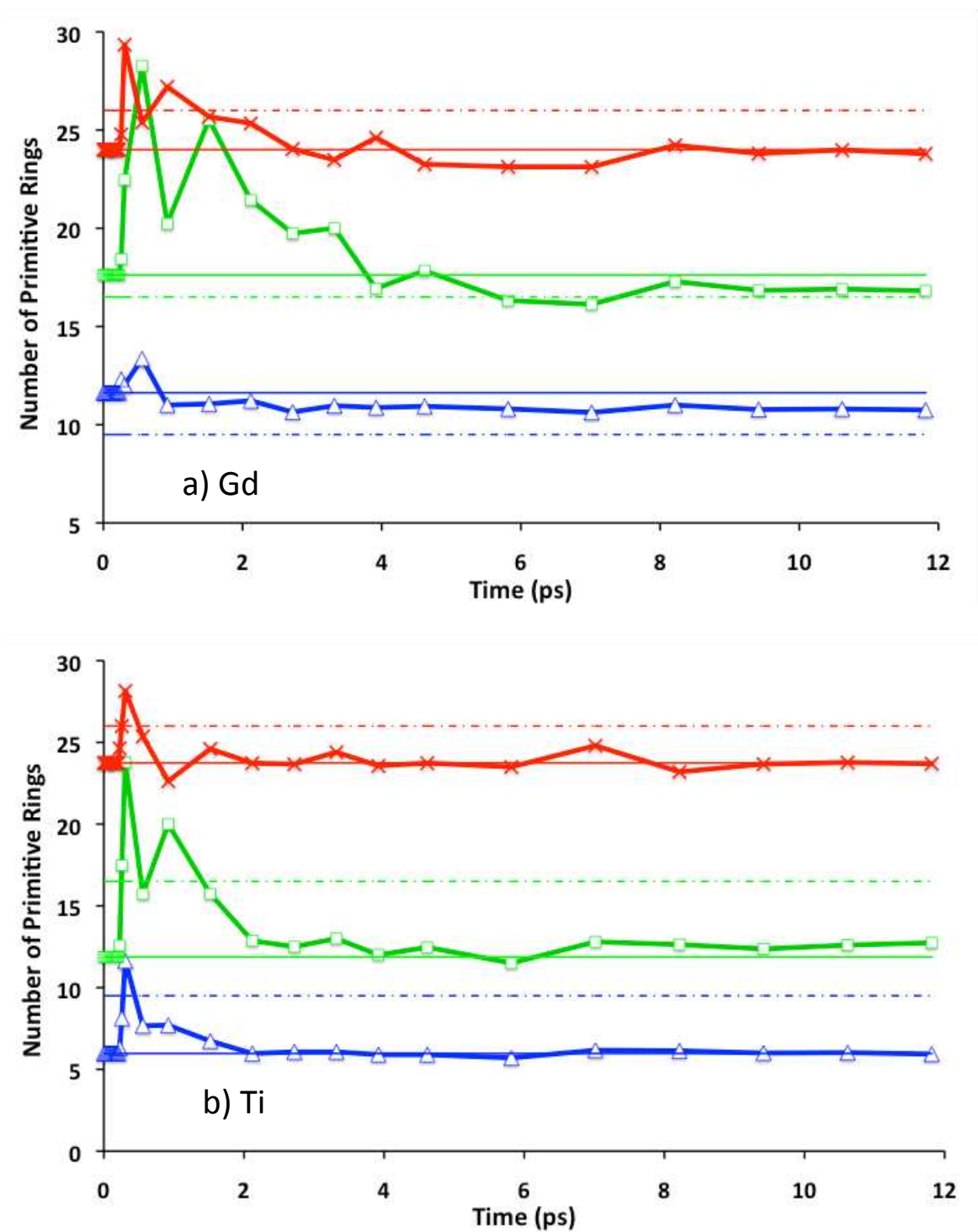


Figure 8 Variations in CT signature with simulation time for 4,6 and 8-ring populations in titanate PYR for a) Gd and b) Ti.

So overall, from both of the Steinhardt and CT analyses it appears that in the early stages of the cascade (< 2 ps), there is extensive rearrangement of atoms, and their connectivity changes during these highly non-equilibrium initial conditions. After 4 ps Steinhardt analysis observes the onset of pyrochlore formation, i.e. the connectivity relationship of the structure is formed before polyhedral relaxation leading to long-term stable structures. One possibility is that initially the topologically more rigid $[\text{TiO}_6]$ octahedra (with fewer degrees of freedom and stronger bonds) dictate the rearrangement and the $[\text{GdO}_x]$ polyhedra distort to maintain connectivity. 25 ps after our single cascade, we are left with anion disorder but also with substantial reversion to the pyrochlore. In this context we note damage accumulation models such as the Direct-Impact/Defect-Stimulated (D-I/D-S) model (see for a review ref. ⁴¹) predict a sigmoidal nature to the accumulation of radiation damage in a titanate ceramic - a certain irradiation dose is needed before significant accumulation of damage. In metamict titanite (CaTiSiO_5) X-ray absorption near-edge structure spectroscopy (XANES)⁴² has revealed five-fold coordinate Ti and this has also been noted in simulations of zirconolite ($\text{CaZrTi}_2\text{O}_7$).²² In these multiple, rather than, as here, single cascade simulations²² the formation of $[\text{TiO}_x]$ polyhedral edge-sharing chains is observed and these possibly hinder recovery.

Radiation Damage in $\text{Gd}_2\text{Zr}_2\text{O}_7$

We start once more with the Steinhardt parameters Q_i , plotted in Figures 9a (entire simulation cell) and 9b (damaged region, defined similarly to Ti). These show that the timescales of transient structural changes and subsequent healing are faster than those for the Ti compound. Figure 9a shows that the extent of formation of the anion-disordered structure ADP is smaller than in the Ti analogue, reaching a maximum of less than 1% rather than 5%. Some of the ADP partially heals to INT1. Unlike the Ti compound there is almost no reversion of ADP to pyrochlore with time. These observations are consistent with high oxygen mobility, a more stable ADP structure and a rapid healing of the anion sub-lattice while local temperatures are elevated in the vicinity of the PKA track. In total, after a single cascade, there are only a small number of cation anti-site defects formed and very little DF is formed.

Figure 9b is analogous to Figure 9a but considers only a highly damaged part of the simulation cell, specifically, once again, a cubic cell of side 14 Å centred on the PKA track where the cascade possessed the greatest cross-sectional area. The enhanced oxygen mobility is evident once more since in this region 100% conversion to ADP is virtually immediate. Local ingrowth of INT1 begins after a few ps of structural disorder and the growth of this phase almost exactly complements the reduction in ADP. There is no reversion to PYR. Contrary to our initial expectations, very little DF is seen; there is too little cation disorder. The extra disorder needed to randomise both anions and cations is energetically unlikely with only a single cascade.

Figure 10 shows snapshots of the cascade simulation with respect to time, where spheres with average Q_1 values suggesting predominantly INT1 are shown in yellow, and those showing ADP in orange. Each sphere has a radius equal to that of the secondary cut-off, equal to 12 Å. Consistent with Figure 9 we see the formation of ADP and then partial formation of INT1. In general INT1 lies on the outside of the ADP regions, on the boundary with PYR, as expected. The sizes of the damaged regions are less than for the Ti compound in Figure 8.

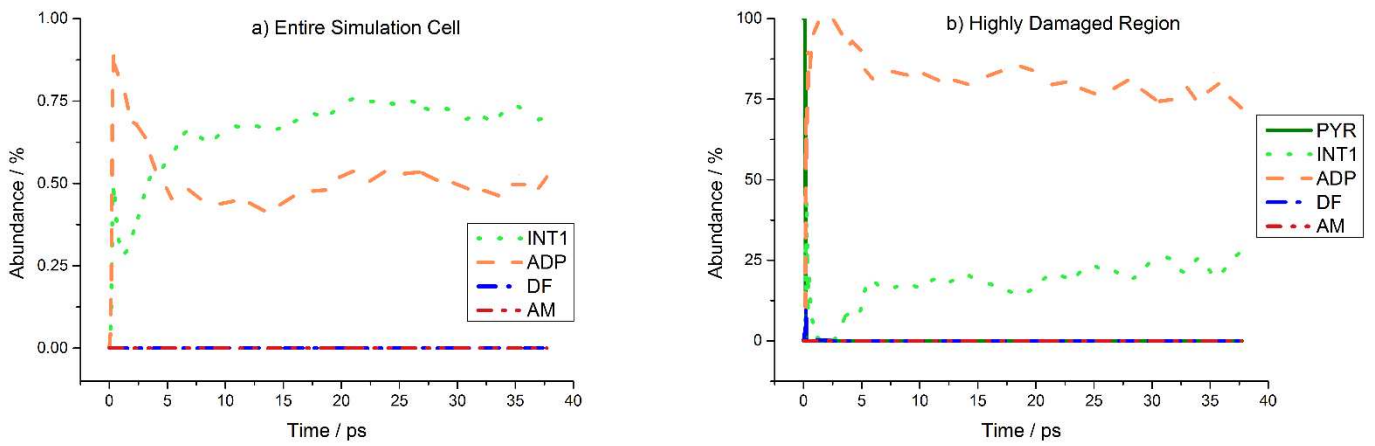


Figure 9 The relative abundance of pyrochlore (PYR), anion-disordered pyrochlore (ADP), defect fluorite (DF), the intermediate (INT1) and the amorphous (AM) structures in the simulated damage cascade in $\text{Gd}_2\text{Zr}_2\text{O}_7$ as a function of time (a) in the entire simulation cell (b) in a cubic box of side 14 \AA taken from the cell as described in the text. PYR is not shown in frame (a) since its abundance is never below 99%.

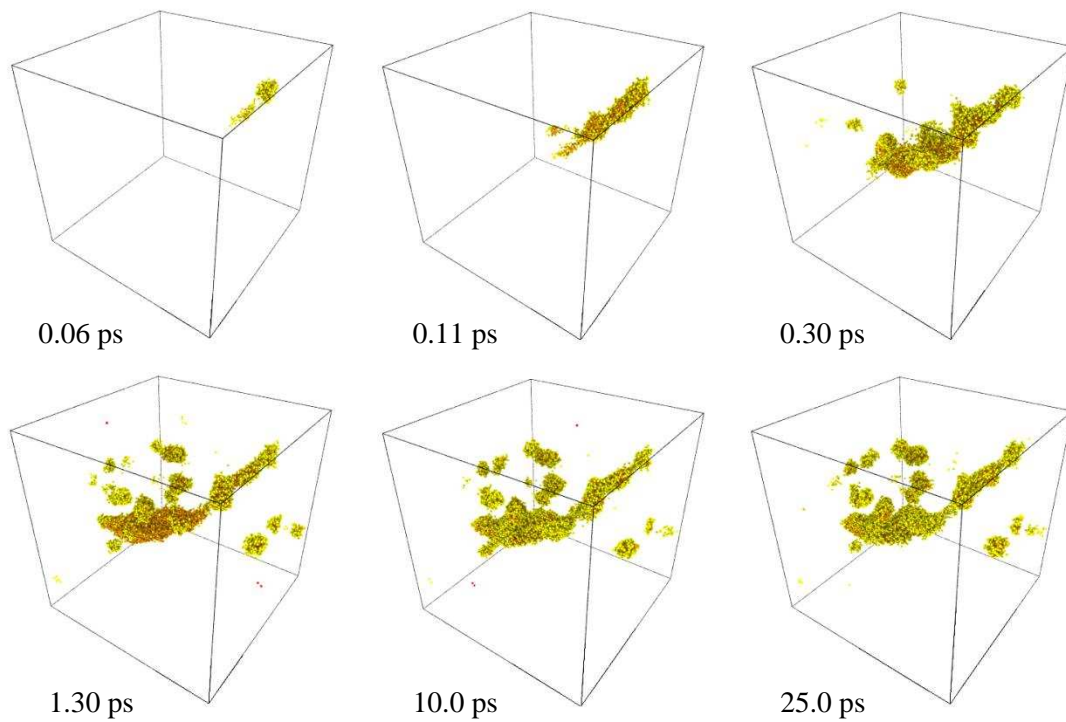


Figure 10. Analysis of selected frames of the cascade in $\text{Gd}_2\text{Zr}_2\text{O}_7$ at 0.06, 0.11, 0.30, 1.30, 10 and 25 ps. These times are the same as for $\text{Gd}_2\text{Ti}_2\text{O}_7$ in Figure 7. Each orange sphere represents a spherical region with a radius of 12 Å in which the dominant structure is ADP as indicated by the Q_1 values. The yellow spheres correspond to the regions identified as INT1.

Figure 11 shows the variation in CT signatures for the damaged region in Zr-PYR, which differs from that of the titanate in two ways – firstly, there is much less topological change in the first 2 ps, and the length of this transient phase is much shorter than in Ti-PYR. Secondly CT analysis shows a wholesale shift in topological signature away from that of PYR, and, consistent with the Steinhardt analysis, there is no subsequent reversion to pyrochlore. For both cation types, ring populations for 4 and 6-rings remain permanently changed from their initial PYR values. However, a reduction in 8-ring population for Zr is in contrast to that for Gd, where this remains relatively unchanged. All changes in the topological signatures are complete before ~4 ps. In contrast to the titanate, where CT and Steinhardt analyses highlight to distinct parts of the radiation damage process and their differing timescales, in the zirconate high anion mobility drives the changes in structure.

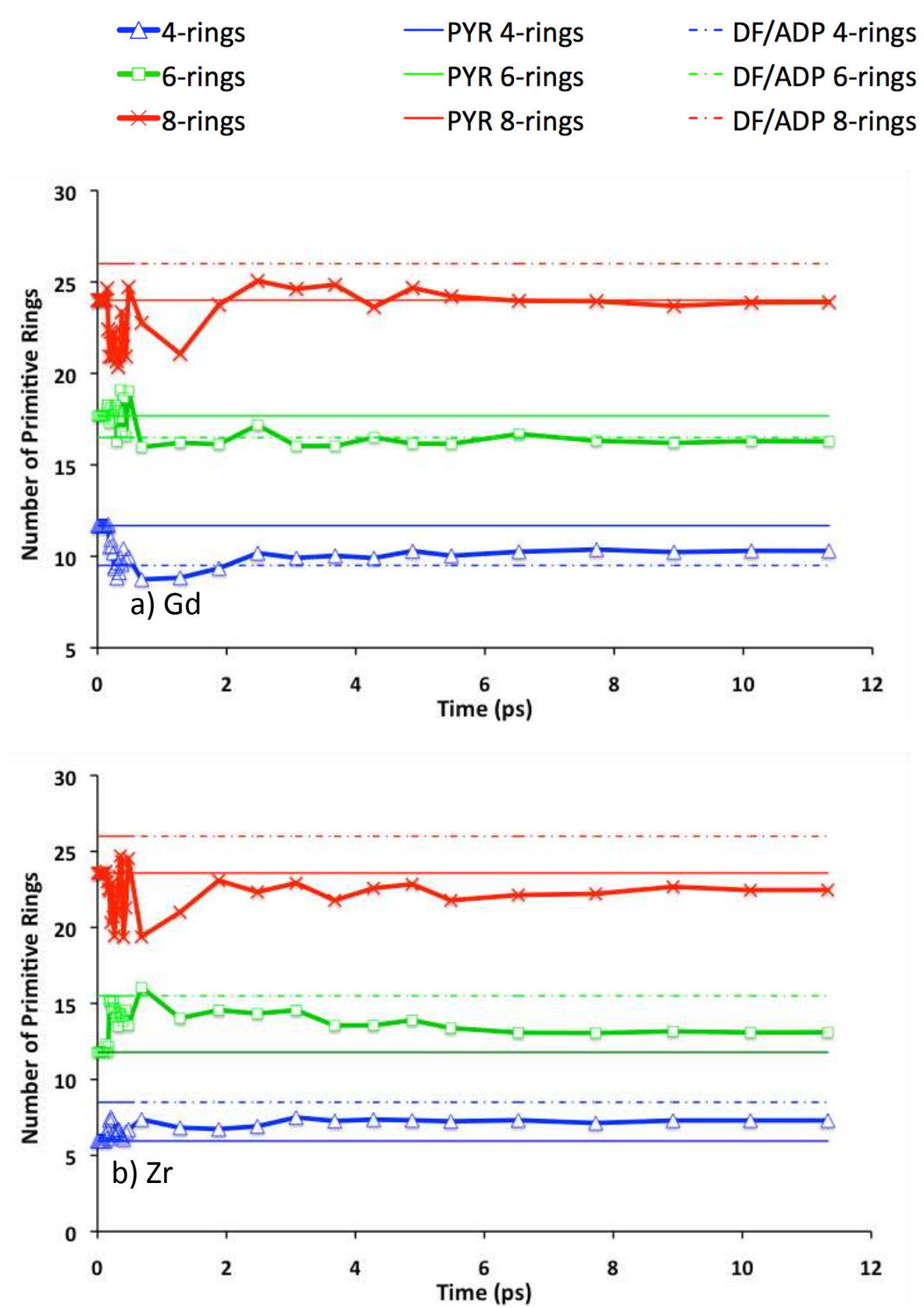


Figure 11 Variations in CT signature with simulation time for 4,6 and 8-ring populations in zirconate PYR for a) Gd and b) Zr

Conclusions

We have applied bond order and connectivity topology analysis methods to the problem of analysing the results of alpha-recoil cascade radiation damage simulations in pyrochlore structured ceramics. For both $\text{Gd}_2\text{Ti}_2\text{O}_7$ and $\text{Gd}_2\text{Zr}_2\text{O}_7$ the techniques are useful and relevant tools that are translationally and rotationally invariant and which do not rely on a particular choice of a reference structure. Results from the Steinhardt and CT analyses are consistent, while often providing complementary information. The Steinhardt analysis can add depth and confidence to structural type identification, since angular arrangements can change significantly even when overall connectivity does not. Both techniques reveal significant localised transient structural changes and changes in the cation-connectivity during the highly non-equilibrium conditions at the start of the cascade. A few picoseconds after the initiation of a single cascade, the connectivity is largely fixed and changes to the CT signatures subside, while the order parameter signatures continue to change. After 4 ps, the titanate pyrochlore reforms, i.e. the connectivity relationship of the structure is formed before polyhedral relaxation leading to long-term more stable structures. In the zirconate there is a shift to the anion disordered system and, in contrast to the titanate, there is no reversion to pyrochlore.

Together, the order parameters and topological methods provide valuable insight into the mechanisms and extent of radiation damage in pyrochlore materials, providing information that cannot be obtained from the traditional methods of analysis and we expect to make extensive use of these in future work.

Acknowledgements

Support from EPSRC is gratefully acknowledged (grants EP/H013814/1, EP/H012230/1 and EP/H012990/1). Mike Stein and Dr. Darragh O'Neill provided valuable assistance with the computation of the Steinhardt order parameters. HRF and KPT would like to thank Prof. Linn Hobbs (MIT) for valuable discussion on topological methods used during the course of this work. The Steinhardt analysis was carried out using the computational facilities of the Advanced Computing Research Centre, University of Bristol - <http://www.bris.ac.uk/acrc/>.

References

- 1 Lumpkin G R 2006 *Elements* **2** 365
- 2 Omel'yanenko B I, Livshits T S, Yudinsev S V, Nikonov B S 2007 *Geol. Ore Deposits* **49** 173
- 3 Ringwood A E, Kesson S E, Ware N G, Hibberson W, Major A 1979 *Nature* **278** 219
- 4 Deschanel X, Peugeot S, Cachia J N, Charpentier T 2007 *Prog. Nuc. Energ.* **49** 623
- 5 Ringwood A E, Oversby V M, Kesson S E 1981 *Nucl. Chem. Waste. Man.* **2** 287
- 6 Vance E R, Lumpkin G R, Carter M L, Cassidy D J, Ball C J, Day R A, Begg B D 2002 *J. Am. Chem. Soc.* **85** 1853
- 7 Wang S X, Begg B D, Wang L M, Ewing R C, Weber W J, Govidan Kutty K V 1999 *J. Mater. Res.* **14** 4470
- 8 Todorov I T, Purton J A, Allan N L, Dove M T 2006 *J. Phys Condens. Mat.* **18** 2217
- 9 Lian J, Wang L M, Haire R G, Helean K B, Ewing R C 2004 *Nucl. Instr. Meth. B* **218** 236
- 10 Mazzi F, Munno R 1983 *Am. Mineral.* **68** 262
- 11 Rossell H J 1980 *Nature* **283** 282
- 12 Ewing R C 2011 *Mineral. Mag.* **75** 2359
- 13 Sickafus K E, Grimes R W, Valdez J A, Cleave A, Tang M, Ishimaru M, Corish S M, Stanek C R, Uberuaga B P 2007 *Nat. Mater.* **6** 217
- 14 Sickafus K E, Minervini L, Grimes R W, Valdez J A, Ishimaru M, Li F, McClellan K J, Hartmann T 2000 *Science* **289** 748
- 15 Devanathan R., Weber W.J., Gale J.D 2010 *Energy Environ. Sci.* **3** 1551
- 16 Sattonnay G, Tetot R 2014 *J. Phys. Condens. Mat.* **26** 05540
- 17 Wang X J, Xiao H Y, Zu X T, Weber W J 2013 *J. Mater. Chem. C* **1** 1665
- 18 Chartier A, Van Brutzel L, Crocombette J P 2012 *Nucl. Instr. Meth. B* **286** 154
- 19 Moll S, Sattonnay G, Thome L, Jagielski J, Decorse C, Simon P, Monnet I, Weber W J 2011 *Phys. Rev. B* **84** 064115
- 20 Chartier A, Meis C, Crocombette J P, Weber W J, Corrales L R 2005 *Phys. Rev. Lett.* **94** 025505
- 21 Davoisne C, Lee W E, Stennett M C, Hyatt N C, Peng N, Jeynes C 2010 *Ceram. Trans.* **222** 3
- 22 Foxhall H R, Travis K P, Hobbs L W, Rich S C, Owens S L 2013 *Phil. Mag.* **93**:4 328
- 23 Mulroue J, Morris A J, Duffy D M 2011 *Phys. Rev. B* **84** 094118
- 24 Purton J A, Allan N L 2002 *J. Mat. Chem.* **12** 2923
- 25 Devanathan R, Weber W J 2005 *J. App. Phys.* **98** 086110
- 26 Todorov I T, Allan N L, Purton J A, Dove M T, Smith W 2007 *J. Mat. Sci.* **42** 1920
- 27 Trachenko K, Zarkadoula E, Todorov I T, Dove M T, Dunstan D J Nordlund K 2012 *Nucl. Instr. Meth. B* **227** 6
- 28 Steinhardt P J, Nelson D R, Ronchetti M 1983 *Phys. Rev. B* **28** 784
- 29 Gupta P K, Cooper A R 1990 *J. Non. Cryst Solids* **123** 14
- 30 Tuller H 1994 *J. Phys. Chem. Solids.* **55** 1393
- 31 Gunn D S D, Allan N L, Foxhall H, Harding J H, Purton J A, Smith W, Todorov I T, Travis K P 2012 *J. Mat. Chem.* **22** 4675
- 32 Deng H F, Bacon D J 1996 *Phys. Rev. B* **43** 11376
- 33 Wigner E, Seitz F 1933 *Phys. Rev.* **43** 804
- 34 Wigner E, Seitz F 1934 *Phys. Rev.* **46** 509
- 35 Todorov I T, Smith W 2004 *Phil. Trans. Roy. Soc. A* **362** 1835
- 36 Moroni D, ten Wolde P R, Bolhuis 2005 *Phys. Rev. Lett.* **94** 235703
- 37 Chua A L S, Benedek N A, Chen L, Finnis M W, Sutton A P 2010 *Nature Mat.* **9** 418
- 38 Morse PM, Feshbach H 1953 *Methods of Theoretical Physics* (New York:McGraw-Hill)
- 39 Lechner W, Dellago C 2008 *J. Chem. Phys.* **129** 114707
- 40 Mariani C S, Hobbs L W 1990 *J. Non Cryst. Solids* **119** 269
- 41 Weber W J, Zhang Y, Wang L 2012 *Nucl. Instr. Meth. B* **277** 1
- 42 Farges F 1997 *Am. Mineral.* **82** 44